Modelling, Analysis, and Optimisation of a Miniaturized Parallel Robot with Soft Joints for High-Speed Real-Time Control

Maxence Leveziel, Guillaume J. Laurent, Michael Gauthier, Redwan Dahmouche

***Abstract*—Classical mechanical joints limit the miniaturization level of mechanisms and robots. Soft joints provide a promising alternative as they can be highly miniaturized. Moreover, they can eliminate backlash and improve robotic precision. However, achieving high accuracy with soft joints requires precise mathematical models, often based on Finite Element Models (FEM). Although FEM offers high accuracy, it is too computationally intensive for high-speed, real-time applications.**

In this paper, we propose cubic soft joints as an alternative to spherical joints for miniaturized parallel robots. We demonstrate that these joints effectively approximate the behavior of spherical joints, enabling a simplified kinematic model that significantly reduces computational load without significantly compromising accuracy. This approximate model also simplifies the analysis of the robot's singularity and workspace, as well as its optimization. Experimental results show minimal differences between the proposed model and more complex FEM models, yet the proposed approach is thousands of times faster, making high-speed, real-time control of such deformable mechanisms feasible. This advancement facilitates the development of complex, miniaturized robotic architectures with enhanced dexterity and manipulation capabilities.

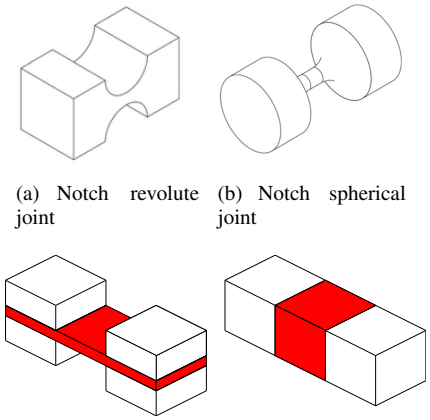

(a) Notch revolute joint (b) Notch spherical joint

(c) Laminated soft revolute joint (d) Cubic soft spherical joint

Fig. 1. Examples of compliant joints and their soft joint counterparts (the red parts represent soft materials).

Statements and Declarations

Funding: This work was funded by the Grand Besançon Métropole, the French ANR project MiniSoRo (ANR-19-CE10-0004), and by EUR EIPHI program (ANR-17-EURE-0002). This work has been partly supported by the French ROBOTEX network (TIRREX ANR-21-ESRE-0015) and its FEMTO-ST technological facility CMNR. This work was carried out in part within the french RENATECH network and its FEMTO-ST technological facility MIMENTO.

I. Introduction

The miniaturization of components, which makes devices smaller and more efficient, necessitates the handling of microcomponents for various tasks, such as biological cell manipulation and sorting, the micro-assembly of medical devices, and more. Several robotic handling tools have been developed based on various micromanipulation principles [1], [2], [3], but they still lack dexterity, precision, and speed.

Micromanipulation and microassembly operations typically require the use of micro-grippers or micro-tweezers. Currently, most micro-tweezers are mounted on decimetre-scale robotic manipulators [4], [5]. These solutions remain cumbersome, exhibit high inertia compared to the manipulated objects, and thus reduce overall performance, particularly in terms of manipulation speed. Reducing the size of the robot itself and its tools is essential to enhancing performance and significantly increasing manipulation efficiency [6].

All Authors are with the FEMTO-ST Institute, Université Marie et Louis Pasteur, CNRS, SupMicroTech-ENSMM, Besançon, France.

The main obstacle to the miniaturization of mechanisms and, by extension, robots, is the difficulty of miniaturizing mechanical joints. Traditional mechanical joints, such as revolute and spherical joints, are not easily manufacturable at small scales. A common approach is to replace standard joints with compliant ones, which can be achieved through local thinning of a single material or by using two materials with different elastic moduli.

The local thinning approach employs the same material for the entire mechanism, making it a monolithic part, as shown in Fig. 1(a) and 1(b). Various geometries have been proposed, with the main advantage being that the manufacturing process does not require assembly [7], [8]. However, mechanical constraints are concentrated in a small region, which limits the joint's travel range. One way to achieve larger deflections is to transition from notches to continuous deformations along leaf springs [7], [9]. This distributes stress along the beam, allowing for greater travel ranges. However, leaf springs are often bulky, making them unsuitable for miniaturization.

Another approach to increasing joint travel range is the use of soft joints. These compliant mechanisms leverage differences in elastic moduli between materials. Two primary types of soft joints are commonly used for miniature robots. The first type is manufactured using a laminating process [10] (see Fig. 1(c)), which is particularly well-suited for revolute joints. However, designing spherical joints using this method requires placing multiple hinges in series, which increases bulkiness, reduces travel range, and may induce undesirable gimbal lock effects. The second type of soft joint involves embedding elastomeric materials into a rigid structure via 3D

printing or molding (see Fig. 1(d)). This technique enables the design of joints with diverse geometries, allowing for the creation of miniature revolute or spherical-like joints [11], [12], [13], [14], [15], [16]. The fabrication of such joints using photolithography and molding has already been demonstrated [17], [18].

The design of soft joints for miniature robots must meet several requirements: the joints must be manufacturable and compact, they should allow for large travel ranges, and their behavior must be predictable within a reasonable computational time. Since the deformation of soft joints relies on continuum mechanics, achieving real-time computation is a challenge. Indeed, some high-speed miniature robots require control frequencies of several hundred hertz [19], [16], making it extremely challenging to compute the kinematic model of the controlled robot in real time.

For instance, MiGriBot's actuators [16] have a response time of approximately 8 ms and a sampling period of less than 0.5 ms, enabling the robot to achieve a pick-and-place cycle time of under 85 ms. Finite Element Models (FEM) are typically incompatible with such speeds, preventing their use in real-time applications. To circumvent this limitation, robot trajectories are computed offline. However, this approach restricts the robot from adjusting its trajectory based on the real-time positions of manipulated objects, even when using additional sensors such as cameras. This limitation can be particularly problematic at small scales, where precise object positioning is challenging. Therefore, an alternative model capable of high-speed computation without significantly compromising accuracy would be highly beneficial.

In this paper, we analyze the accuracy and speed of different modeling approaches for cuboid soft joints in miniature robots. Additionally, we investigate the most suitable form factor for soft joints and derive Rigid-Body models for MiGriBot that achieve both high speed and accuracy. Specifically, we demonstrate that the proposed model is more than 18,000 times faster than FEM models while being less than 1% less accurate than the most precise FEM model.

Thus, the main contribution of this paper is to analyze and develop alternative models for MiGriBot, and more generally for robots with soft cuboid joints, that enable real-time trajectory generation, adaptation, and control.

The next section presents different approaches to soft joint modeling, while Section III focuses on modeling cuboid soft joints and analyzing the impact of size ratio on model accuracy. Section IV derives the various models and analyzes MiGriBot's kinematic architecture, optimizing certain design parameters in Section V. Experimental results and conclusions are presented in Sections VI and VII, respectively.

II. Modeling of Soft Joints

A. Finite Element Model

The Finite Element Method (FEM) is the standard tool for analyzing the deformation of continuum media. It involves dividing the medium into multiple small sub-elements (mesh). Each element is modeled individually using linear or quadratic interpolation functions, and their interactions are combined to determine the overall deformations.

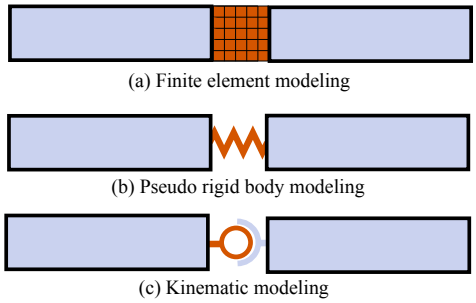

Fig. 2. Three types of models: the finite element model, the pseudo-rigid-body method, and the rigid-body method.

The design of most soft robots relies on FEM, utilizing commercial software such as ABAQUS©, ANSYS©, and COMSOL©, as well as academic tools like SOFA [20]. FEM can be employed to model soft joints deforming within a rigid structure, as illustrated in Fig. 2(a). It accurately predicts the deformation of soft joints subjected to large displacements. However, its computational time and memory usage are substantial and directly related to the number of elements in the mesh. The key question is to assess the added value of FEM in terms of accuracy versus computational cost for mechanisms incorporating soft joints.

One possible simplification is to use 1D elements. In this case, a soft joint is represented by one or more beam elements, depending on its aspect ratio. If only one beam element is used, the model closely resembles the pseudo-rigid-body method.

B. Pseudo-Rigid-Body Model

The pseudo-rigid-body method is a lumped-parameter approach that approximates a flexible body as a series of rigid bodies connected by elastic discrete joints [21]. The degrees of freedom at the joints account for the deformation modes of the flexible unit, while springs and dampers capture its stiffness and damping properties. In the case of a soft joint, none of the degrees of freedom are constrained. The soft joint can be represented by torsional and/or translational springs connecting adjacent rigid links (Fig. 2(b)).

The relationship between the wrench and the deformation of the joint is given by a generalized stiffness matrix K:

$$\begin{pmatrix} F \\ M \end{pmatrix} = K \cdot \begin{pmatrix} D \\ \Theta \end{pmatrix} \tag{1}$$

The coefficients of the stiffness matrix are defined based on the geometry of the joint.

The pseudo-rigid-body method has been extensively applied to compliant mechanisms. It has also been used to model soft joint mechanisms, including the MilliDelta [19], the HSC joint [13], leg mechanisms [11], and miniature walking robots [12]. These studies demonstrate that pseudo-rigid-body models provide accurate predictions for small deformations while remaining computationally efficient. The key question is to determine the extent to which the pseudo-rigid-body method remains suitable for mechanisms with soft joints undergoing large deformations.

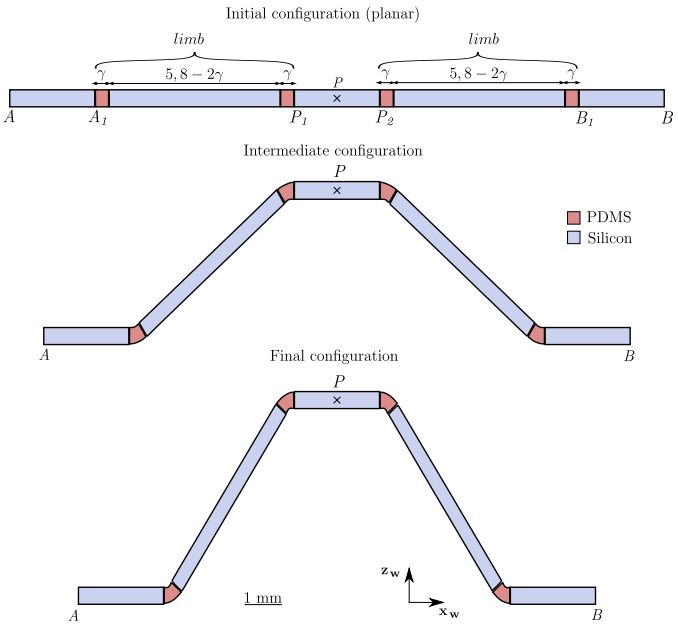

Fig. 3. Planar mechanism with four soft joints. This figure provides the dimensions and materials used for cubic soft joints (γ = 400 µm; size ratio = 1). Each part of the mechanism has a square cross-section with a width of 400 µm.

C. Rigid-Body Model

The simplest approach is to model soft joints as ideal spherical joints. This method has been successfully applied in controlling the mini-RCM manipulator [22] and the portable haptic device [23], both of which utilize revolute laminated soft joints.

The main advantages of this approach are its ease of implementation and compatibility with conventional robotic tools (e.g., direct and inverse modeling, singularity analysis, and manipulability). Another significant benefit is its low computational cost. However, this method is a rough approximation of the actual behavior of soft joints. Therefore, it is crucial to evaluate the loss of accuracy compared to high-fidelity FEM models.

III. Modeling of Soft Cuboid Joints

To compare different modeling approaches for soft cuboid joints and select an appropriate one, we analyze the behavior of a simple mechanism composed of such joints. We consider a miniature planar mechanism consisting of five rigid links and four soft joints, designed with realistic dimensions based on the microfabrication process introduced in [18]. We simulated the behavior of the soft joints using seven different models on the same computer with the same set of parameters. The objective is to assess the advantages and disadvantages of each model concerning the software used, mesh size, computational time, and accuracy in predicting motion.

A. Description of the Numerical Benchmark

The mechanism is illustrated in Fig. 3. In its initial configuration, the distance between A and B is 19.1 mm. Each segment of the mechanism has a square cross-section with a width of 400 µm. The platform (central part of the mechanism), denoted by its inertial center P, has a fixed length of 2.5 mm. The distances between A and A_1, and between B and B_1, are also constant at 2.5 mm. The distances between A_1 and P_1, and between B_1 and P_2, are 5.8 mm in the absence of external forces. The length ratio of the soft elements in these parts varies accordingly.

The two external links are actuated along the X-axis, allowing the distance AB to be adjusted. The planar mechanism operates symmetrically along the x_w axis, meaning that points A and B move closer together as AB varies. The displacement of P in the vertical direction is observed. The distance AB is reduced from 19.1 mm to 15.1 mm with a constant step size of 20 µm. To initiate the buckling of the mechanism upwards, a small force along z_w is applied during the initial simulation steps.

TABLE I
Mechanical properties of silicon and PDMS used in the modeling

Material	Young's Modulus	Poisson's Ratio
PDMS	1.4 MPa	0.49
Silicon	160 GPa	0.29

Following the microfabrication process, the rigid links are made of silicon, while the soft joints are composed of polydimethylsiloxane (PDMS). The mechanical properties, including Young's modulus and Poisson's ratio for both materials, are provided in Table I [24], [25], [26]. From this table, it is evident that the Young's modulus of silicon is five orders of magnitude higher than that of PDMS. Additionally, the Poisson's ratio of PDMS is close to 0.5, indicating that it is nearly incompressible. These two factors can lead to numerical instabilities in finite element modeling (FEM) and slow down convergence.

B. Definition of the Models

In this study, we assume the following hypotheses: we focus on the static deformations of the joints without considering dynamic behavior. We also assume that the material properties are isotropic and elastic and that the soft joints are cuboids with varying aspect ratios.

We consider three different modeling approaches: FEM with 3D elements, FEM with 1D beam elements, and a rigid-body model. For FEM, we use both ANSYS© and SOFA frameworks, while MATLAB© is used for the rigid-body model.

The models must account for both large bending and axial compression of the soft joints. In ANSYS©, the PDMS parts are modeled using two types of 3D elements (tetrahedral and hexahedral) with regular meshing and two different element sizes: 40 µm and 80 µm. The silicon parts are modeled with a hexahedral mesh consisting of 200 µm elements. All 3D elements use quadratic interpolation functions. The model A_{3Dfine} is the most accurate and serves as the reference for all comparisons.

We also model the soft joints using SOFA with hexahedral elements of the same mesh sizes, but with linear interpolation

TABLE II
DESCRIPTION OF THE SEVEN MODELS, INCLUDING TYPE, SOFTWARE, AND MESHING PARAMETERS.

Model		**Software**	**Meshing Parameters**	
Name	**Type**		**PDMS Parts**	**Silicon Parts**
A_{3Dfine}	FEM 3D	ANSYS©	Tetrahedral elements of 40 µm	Hexahedral elements of 200 µm
$A_{3D0.04}$	FEM 3D	ANSYS©	Hexahedral elements of 40 µm	Hexahedral elements of 200 µm
$A_{3D0.08}$	FEM 3D	ANSYS©	Hexahedral elements of 80 µm	Hexahedral elements of 200 µm
$S_{3D0.04}$	FEM 3D	SOFA	Hexahedral elements of 40 µm	Rigid elements
$S_{3D0.08}$	FEM 3D	SOFA	Hexahedral elements of 80 µm	Rigid elements
S_{1D}	FEM 1D	SOFA	Beam elements of 400 µm	Rigid elements
$C_{spherical}$	Rigid-body	MATLAB©	Ideal spherical joints	Rigid elements

functions. In SOFA, the silicon parts are represented as rigid bodies, which helps avoid issues arising from vastly different elastic moduli.

Additionally, the soft joint is modeled using 1D beam elements through the BeamAdapter plugin in SOFA. Beam elements exhibit a linear response to loads, as described in Eq. (1), and their stiffness matrix is provided in Appendix A.

For cubic soft joints (size ratio of 1), a single beam element per joint is used, making this model closely resemble a pseudo-rigid-body model, differing only in the calculation of beam length in relation to compression strain.

Finally, we compute the forward kinematics of the mechanism under the assumption of ideal revolute joints. The coordinates of points A_1, P_1, P_2, and B_1 are provided in Appendix B.

C. Model Comparison for Cubic Soft Joints

To conduct a comprehensive study, we tested seven models of cubic soft joints. The characteristics of these models are summarized in Table II. The comparison is based on two criteria: the total computation time and the average error along the trajectory relative to the reference model. The simulations were performed on a computer equipped with an INTEL© 8-core i5-10400H CPU running at 2.6 GHz with 16 GB of RAM.

We first compared the models for cubic soft joints, followed by an analysis of different size ratios of the soft joints. The cubic soft joints have a length of 0.4 mm (size ratio of 1), while the rigid silicon parts are 5 mm long. Figure 4 shows the position z_w of the platform as a function of the distance AB for each model. The results indicate that for cubic soft joints, the different models produce similar results. Specifically, for a reduction of 4 mm in the AB distance, the relative error remains below 5%. The rigid-body model $C_{spherical}$, shown in black in the figure, slightly overestimates the platform's elevation, whereas the SOFA models $S_{3D0.04}$, $S_{3D0.08}$, and S_{1D}, shown in red, tend to underestimate it. Notably, the three ANSYS models, A_{3Dfine}, $A_{3D0.04}$, and $A_{3D0.08}$, yield similar results regardless of mesh refinement.

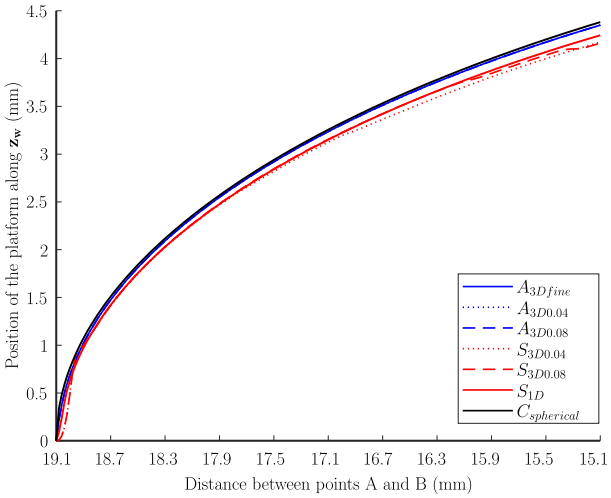

Fig. 4. Displacement in the z_w direction of point P as a function of the distance AB, obtained with each model for cubic soft joints (size ratio = 1).

Another critical factor in the context of robot control is computation time. The rigid-body model $C_{spherical}$ had the shortest simulation time at 0.31 ms. The SOFA beam model S_{1D} took 5.75 s. The 3D FEM models $S_{3D0.08}$ and $A_{3D0.08}$, which use 80 µm hexahedral elements, required 35.46 s and 508 s, respectively. Simulations with 40 µm elements, i.e., the $S_{3D0.04}$ and $A_{3D0.04}$ models, took 421.9 s and 1324 s, respectively. Consequently, the $C_{spherical}$ model is over 18,000 times faster than the beam model S_{1D} and more than 1 million times faster than the fastest FEM model.

These results demonstrate that for this planar mechanism and in the case of cubic soft joints, the rigid-body model $C_{spherical}$ provides an excellent trade-off. Its relative error remains below 1%, while its computational time is significantly shorter than that of the other models.

D. Optimal Size Ratio of the Cuboid Soft Joint

To determine the optimal size ratio (length-to-thickness ratio) of the cuboid soft joint, we analyzed the accuracy of

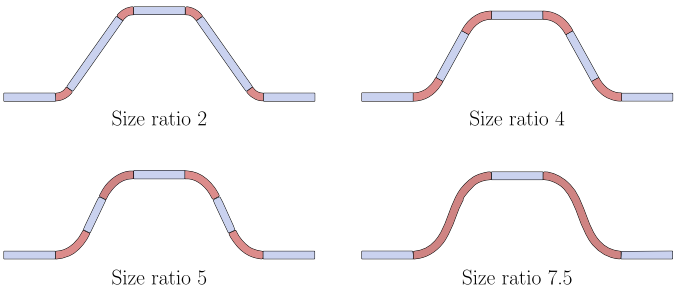

Joint Size Ratio	Joint Length γ (mm)	Silicon Length (mm)
1	0.4	5
2	0.8	4.2
4	1.6	2.6
5	2.0	1.8
7.5	2.9	0

Fig. 5. Definition of the study cases used to analyze the impact of joint length on model performance.

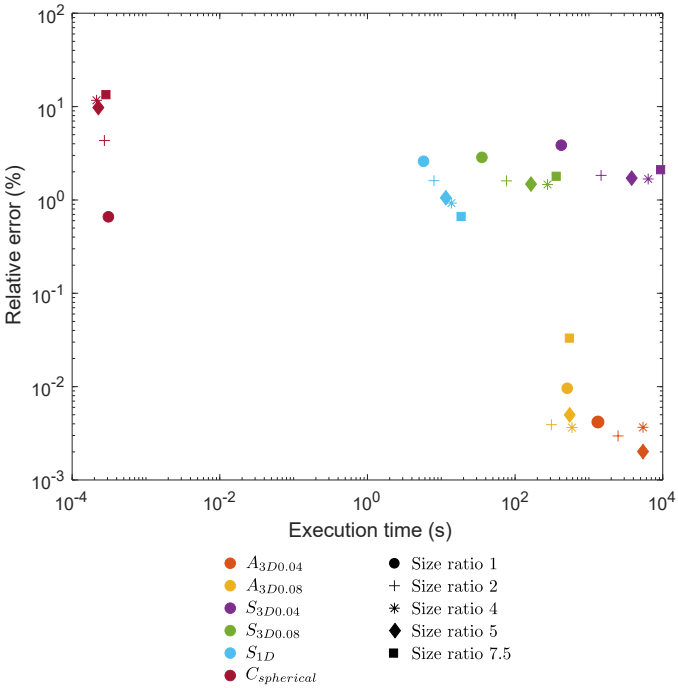

Fig. 6. Comparison of models for different size ratios of soft joints.

different models as a function of the soft joint's size ratio. We considered five different geometries (see Fig. 5), where γ denotes the length of each soft joint within the limb. In this study, γ varies between 0.4 mm and 2.9 mm. In the latter case, the limb consists entirely of soft elements. The five cases are defined by the joint size ratios presented in Table 5.

For each model, we compared computational time and the relative error with respect to the reference model A_{fine}. Figure 6 illustrates the average relative error of all models alongside their corresponding execution times. This representation highlights three main groups of models and software.

If computational time is not a constraint, the most accurate models are the FEM ones with small 3D elements (red markers), as they capture the complex deformations of soft joints. For a size ratio of 1 (circular markers), the figure confirms that the rigid-body model provides a good balance between

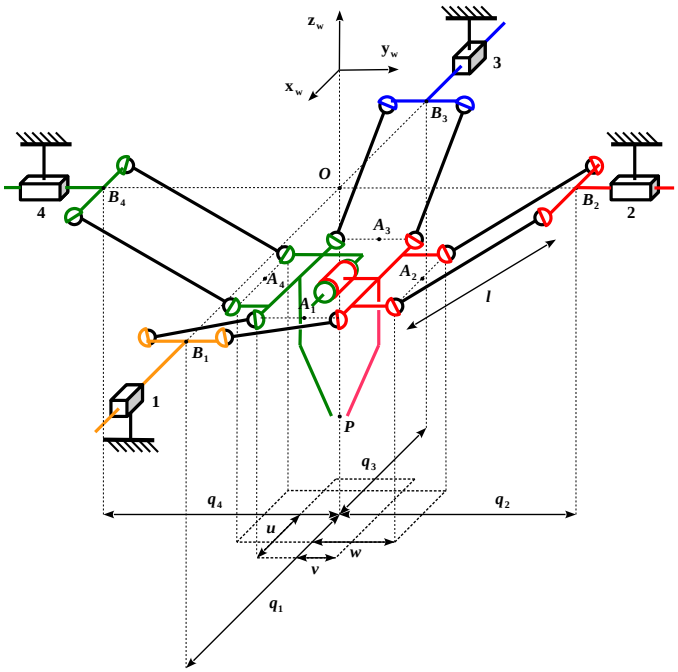

Fig. 7. Kinematic scheme of the MiGriBot, a 4-DoF parallel manipulator.

accuracy and computational efficiency. For other aspect ratios, SOFA models with 1D beam elements (cyan markers) achieve relative errors below 2% while reducing computational time by a factor of 100 compared to ANSYS models (yellow and red markers). Notably, SOFA models using 3D elements do not outperform those using 1D beam elements. Thus, SOFA models with 1D beam elements present a highly effective trade-off for non-cubic, slender soft joints.

In this section, we observed that the fastest FEM model required 5.75 s, which is too slow for real-time trajectory generation in high-speed robotics, including MiGriBot (where response time $<$ 10 ms and cycle time $<$ 100 ms are required). Furthermore, the rigid-body model exhibited only a 1% error compared to the finest FEM model, which is comparable to the errors of coarser FEM models while being significantly faster (0.31 ms). Additionally, a size ratio of 1 (a cube) was found to yield the highest accuracy. Therefore, the combination of a rigid-body model and a size ratio of 1 appears to be a relevant trade-off for real-time control and trajectory adaptation in ultra-high-speed miniaturized robots, particularly in MiGriBot. In the next section, we apply these findings to MiGriBot.

IV. Rigid-body Model and Kinematic Analysis of the MiGriBot

Figure 7 defines the geometrical parameters of the mechanism:

- u is the half-length of the platform in the $\mathbf{x_w}$ direction,
- w is the half-width of the platform in the $\mathbf{y_w}$ direction,
- v is the distance between the axis of the revolute joint and the line passing through the centers of the opposite spherical joints connected to actuators 1 and 3 ,
- l stands for the length of the limbs.

In order to derive the kinematic models of the MiGriBot, we define the following variables:

- $\mathbf{q} = (q_1, q_2, q_3, q_4)^{\mathrm{T}}$ is the configuration vector of the robot in the joint space where q_i is the linear position of the i$^{\text{th}}$ actuator (equals to the distance between origin O and point B_i),
- $\mathbf{x} = (x_p, y_p, z_p, \theta)^{\mathrm{T}}$ is the pose vector of the end-effector, where x_p, y_p z_p are the coordinates of the platform center point P, and θ is the angle between the right part of the platform and the horizontal plane.

Because of the symmetry of our architecture, only one variable (θ) is sufficient to define the opening/closing movement of the platform. Indeed, the angle between the left (respectively right) part and the horizontal is always the same because legs 1 and 3 are anchored at the same level to the platform. θ is then the half-opening angle of the gripper. When $\theta = 0$, the platform is flat.

To keep constant the distance of the distal spherical joints of limbs 1 and 2 and then ensure the parallelism between the legs, the rotation between the right and left parts of the platform must be small. Indeed, the distance between these spherical joints is equal to $2v\cos(\theta)$ which can be approximated by its first-order Taylor expansion $2v + o(\theta^2)$. In practice, the flexibility of the legs and the joints compensates for the deviations of second order in the range of ten degrees at least.

A. Closure Equations

To write the closure equations, we express the coordinates of the points A_i and B_i in the world frame (see Fig. 7). Using the first-order Taylor expansion around zero for the cosine and sine functions, we get the following coordinates:

$$A_1 = \begin{pmatrix} x_p + u \\ y_p \\ z_p + v\theta \end{pmatrix}, \quad A_2 = \begin{pmatrix} x_p \\ y_p + w \\ z_p + w\theta \end{pmatrix}, \tag{2}$$

$$A_3 = \begin{pmatrix} x_p - u \\ y_p \\ z_p + v\theta \end{pmatrix}, \quad A_4 = \begin{pmatrix} x_p \\ y_p - w \\ z_p + w\theta \end{pmatrix}, \tag{3}$$

$$B_1 = \begin{pmatrix} q_1 \\ 0 \\ 0 \end{pmatrix}, \quad B_2 = \begin{pmatrix} 0 \\ q_2 \\ 0 \end{pmatrix}, \tag{4}$$

$$B_3 = \begin{pmatrix} q_3 \\ 0 \\ 0 \end{pmatrix}, \quad B_4 = \begin{pmatrix} 0 \\ q_4 \\ 0 \end{pmatrix}. \tag{5}$$

Then, the kinematic closure equations can be written:

$$\forall i \in \{1,2,3,4\}, \quad A_iB_i = \left\| \overrightarrow{A_iB_i} \right\| = l. \tag{6}$$

The expansions of the four squared equations are given by:

$$(x_p + u - q_1)^2 + {y_p}^2 + (z_p + v\theta)^2 = l^2, \tag{7}$$

$$(x_p - u - q_3)^2 + {y_p}^2 + (z_p + v\theta)^2 = l^2, \tag{8}$$

$${x_p}^2 + (y_p + w - q_2)^2 + (z_p + w\theta)^2 = l^2, \tag{9}$$

$${x_p}^2 + (y_p - w - q_4)^2 + (z_p + w\theta)^2 = l^2. \tag{10}$$

B. Inverse Kinematics Modeling

In the inverse kinematics problem, it is assumed that the end-effector position (x_p, y_p, z_p) and platform angle θ are known. The purpose is to find the joint positions (q_1, q_2, q_3, q_4).

Due to the presence of squared expressions, the development and separation of the different terms of the different closure equations lead to two possible configurations for each actuator q_i. The solutions of the inverse kinematics of the MiGriBot are then given by:

$$\begin{cases} q_1 = x_p + u + \varepsilon_1\sqrt{l^2 - {y_p}^2 - (z_p + v\theta)^2} \\ q_2 = y_p + w + \varepsilon_2\sqrt{l^2 - {x_p}^2 - (z_p + w\theta)^2} \\ q_3 = x_p - u - \varepsilon_3\sqrt{l^2 - {y_p}^2 - (z_p + v\theta)^2} \\ q_4 = y_p - w - \varepsilon_4\sqrt{l^2 - {x_p}^2 - (z_p + w\theta)^2} \end{cases} \tag{11}$$

with $\varepsilon_i \in \{1, -1\}$.

The assembly constraints allow us to choose the solutions for each actuator that are the farthest from the origin O, i.e. $\varepsilon_1 = \varepsilon_2 = \varepsilon_3 = \varepsilon_4 = 1$.

The closure equations give also a condition for a pose to be in the workspace. To be attainable, a pose $\mathbf{x} = (x_p; y_p; z_p; \theta)$ has to satisfy the following conditions:

$$\begin{cases} {y_p}^2 + (z_p + v\theta)^2 \leq l^2 \\ {x_p}^2 + (z_p + w\theta)^2 \leq l^2 \end{cases} \tag{12}$$

C. Forward Kinematics Modeling

In this section, we assume that joint positions (q_1, q_2, q_3, q_4) are known, and that the end-effector position (x_p, y_p, z_p) and platform angle θ should be determined. In order to find the analytical solution to the forward kinematics problem, we need to make linear combinations of the closure equations. The difference between Eq. (7) and (8) gives the value of x_p as a function of the actuators positions q_1 and q_3:

$$x_p = \frac{q_1 + q_3}{2} \quad \text{if} \quad q_1 - q_3 \neq 2u \tag{13}$$

The case where $q_1 - q_3 = 2u$ corresponds to the fact that the distance between the actuators q_1 and q_3 is the same as the length of the platform and, therefore, the limbs 1 and 3 are perpendicular to the platform. In other words, legs 1 and 3 are both vertical. In this case, x_p is not defined and the manipulator is in a singular configuration (see next section).

In a similar way considering Eq. (9) and (10), we obtain the expression for y_p as a function of the actuators positions q_2 and q_4:

$$y_p = \frac{q_2 + q_4}{2} \quad \text{if} \quad q_2 - q_4 \neq 2w \tag{14}$$

When $q_2 - q_4 = 2w$, the manipulator is also in a singular configuration (see next section).

To get the expressions of z_p and θ is less straightforward than for x_p and y_p. The first step is to get by linear combinations of the four closure equations, the two relations:

$$(7)+(8) \Rightarrow 2(z_p+v\theta)^2 = \underbrace{2l^2-(x_p+u-q_1)^2-(x_p-u-q_3)^2-2{y_p}^2}_{2a} \quad (15)$$

$$(9)+(10) \Rightarrow 2(z_p+w\theta)^2 = \underbrace{2l^2-(y_p+w-q_2)^2-(y-w-q_4)^2-2{x_p}^2}_{2b} \quad (16)$$

Then, the previous equations lead to four algebraic systems that correspond to the four possible assembly modes:

$$(S_1)\begin{cases} z_p+v\theta=\sqrt{a} \\ z_p+w\theta=\sqrt{b} \end{cases} \quad (17)$$

$$(S_2)\begin{cases} z_p+v\theta=-\sqrt{a} \\ z_p+w\theta=-\sqrt{b} \end{cases} \quad (18)$$

$$(S_3)\begin{cases} z_p+v\theta=\sqrt{a} \\ z_p+w\theta=-\sqrt{b} \end{cases} \quad (19)$$

$$(S_4)\begin{cases} z_p+v\theta=-\sqrt{a} \\ z_p+w\theta=\sqrt{b} \end{cases} \quad (20)$$

Among these four systems, (S_3) and (S_4) give an angle θ with values close to π which means that each side of the gripper would be flipped bottom to top. This assembly is not possible because it would requires to cross the legs.

The systems (S_1) and (S_2) correspond to feasible solutions. Indeed, both give the same θ and z_p, but either both positive or negative. (S_1) corresponds to the assembly of the architecture above the plane $O\mathbf{x_w y_w}$, while (S_2) corresponds to the assembly of the architecture below.

To carry out the pick-and-place, the MiGribot must point downwards. So, the solution of the forward kinematics problem is chosen to be (S_2), and is given by:

$$\begin{cases} \theta &= \dfrac{\sqrt{a}-\sqrt{b}}{w-v} \\ z_p &= \dfrac{v\sqrt{b}-w\sqrt{a}}{w-v} \end{cases} \quad (21)$$

D. Singularity Analysis

Considering the rigid-body model, the Jacobian matrices can be derived from the closure equations. The time derivatives of Eq. (7) to (10) leads to:

$$\mathbf{J_x}.\dot{\mathbf{x}} = \mathbf{J_q}.\dot{\mathbf{q}} \quad (22)$$

The matrix $\mathbf{J_x}$ gathers the factors of the end-effector velocity coefficients $\dot{\mathbf{x}} = (\dot{x}_p, \dot{y}_p, \dot{y}_p, \dot{\theta})^{\mathrm{T}}$:

$$\mathbf{J_x} = \begin{pmatrix} x_p+u-q_1 & y_p & z_p+v\theta & v(z_p+v\theta) \\ x_p & y_p+w-q_2 & z_p+w\theta & w(z_p+w\theta) \\ x_p-u-q_3 & y_p & z_p+v\theta & v(z_p+v\theta) \\ x_p & y_p-w-q_4 & z_p+w\theta & w(z_p+w\theta) \end{pmatrix} \quad (23)$$

The matrix $\mathbf{J_q}$ is a diagonal matrix with the factors of the joint speeds $\dot{\mathbf{q}} = (\dot{q}_1, \dot{q}_2, \dot{q}_3, \dot{q}_4)^{\mathrm{T}}$:

$$\mathbf{J_q} = \begin{pmatrix} x_p+u-q_1 & 0 & 0 & 0 \\ 0 & y_p+w-q_2 & 0 & 0 \\ 0 & 0 & x_p-u-q_3 & 0 \\ 0 & 0 & 0 & y_p-w-q_4 \end{pmatrix} \quad (24)$$

When $\mathbf{J_x}$ is invertible, the Jacobian matrix of the MiGriBot can then be obtained by:

$$\mathbf{J} = {\mathbf{J_x}}^{-1}.\mathbf{J_q} \quad (25)$$

The workspace of parallel robots is limited by the presence of singularities, which can be classified into three types [27].

Type I singularities correspond to singularities of matrix $\mathbf{J_q}$. It occurs when the robot reaches either a boundary of its workspace or an internal boundary limiting different aspects of the workspace. Concretely, in these configurations, the robot is not able to generate all its usual DoF.

Type II singularities correspond to singularities of matrix $\mathbf{J_x}$. This kind of singularity produces a loss of control of at least one degree of freedom. Concretely, the platform is locally movable even when all the actuated joints are locked.

Type III singularities correspond to a simultaneous cancellation of the determinant of the matrices $\mathbf{J_x}$ and $\mathbf{J_q}$.

The obtention of the determinant of matrix $\mathbf{J_q}$ from Eq. (24) is straightforward:

$$\det \mathbf{J_q} = (x_p+u-q_1)(x_p-u-q_3) \cdot (y_p+w-q_2)(y_p-w-q_4) \quad (26)$$

Considering equations (13) and (14), it can be rewritten as follows:

$$\det \mathbf{J_q} = \frac{1}{16}(q_3-q_1+2u)^2\,(q_4-q_2+2w)^2 \quad (27)$$

The determinant of matrix $\mathbf{J_x}$ is more complex to calculate and can be factored as:

$$\det \mathbf{J_x} = (w-v)\,(z_p+\theta v)\,(z_p+\theta w) \cdot (q_3-q_1+2u)\,(q_4-q_2+2w) \quad (28)$$

Both equations allow us to identify all the singularities of the MiGriBot. As the zeros of $\det \mathbf{J_q}$ are also zeros of $\det \mathbf{J_x}$, there is no type I singularities.

The first type II singularity is a design singularity which occurs when v is equal to w. It means that an offset is necessary between the position of the spherical joints of the platform. If not, we lose the control of the gripper. This singularity is of course not present if the robot is well designed.

The other type II singularities occur when:

$$z_p = -\theta v \quad \text{or} \quad z_p = -\theta w \quad (29)$$

It corresponds to configurations where a spherical joint of the platform crosses the plane $O\mathbf{x_w y_w}$ as illustrated in Figure 8. In these configurations, we can't control the height and opening on the gripper independently.

As θ is small by assumption and v and w are also small with regards to the workspace height (see next section), these singularities are all located near $z_p = 0$ and do not interfere with the workspace of the manipulator.

The last singularity is type III. It occurs when the legs are perpendicular to the platform (and to the plane $O\mathbf{x_w y_w}$). Because of the symmetries, if one leg is perpendicular to the platform, the opposite leg is also perpendicular. In conclusion, both matrices $\mathbf{J_x}$ and $\mathbf{J_q}$ are singular in only two cases: if $q_1 - q_3 = 2u$ and if $q_2 - q_4 = 2w$. These configurations are illustrated in Figure 8.

As θ, v, and w are small, these singularities are all located at the bottom of the workspace of the manipulator (see next section).

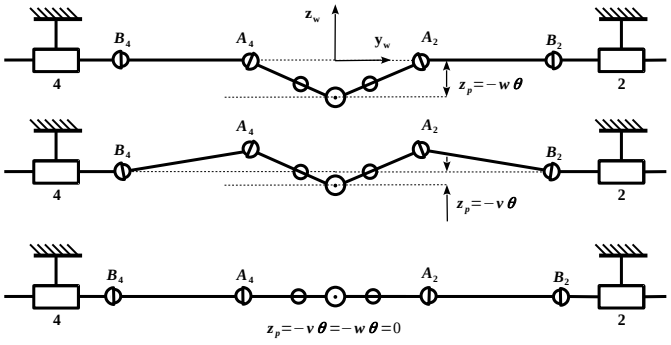

(a) Type II singularities

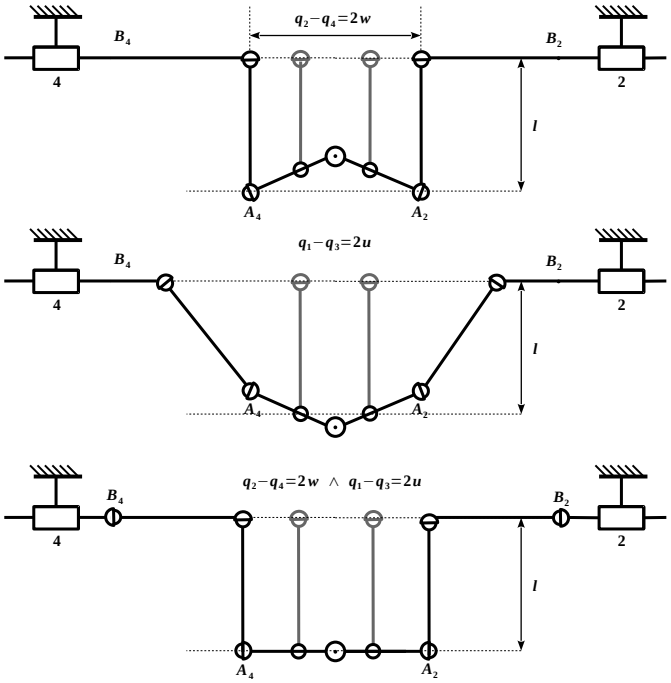

(b) Type III singularities

Fig. 8. Schematic representations of the singularities of the MiGriBot facing downwards. The symmetric singularities exist with the robot facing upwards.

E. Workspace Analysis

The workspace of the manipulator has been numerically computed using its inverse kinematics considering the dimensions of the MiGriBot reported in [16]: u=1.45 mm, w=2.9 mm, v=1.45 mm, and l=5.8 mm. In this section, the linear motors are supposed to have infinite strokes to show the maximal possible workspace. For each Cartesian on a regular sampling is added to the workspace if it fulfills the condition of Eq. 12.

Figure 9 presents the cross-sectional views of the workspace of the manipulator along the Cartesian coordinates x_p, y_p, z_p, considering several angles θ (case (a) to (c)). The workspace in the $O\mathbf{x_w y_w}$ plane is a square whose size depends on z_p. At the maximum, i.e. for $z_p = 0$, the square has a side the length of the leg l. This shows that the length of the legs l is the limiting factor of the workspace width.

In addition, comparing cases (a), (b), and (c), we can see that the θ angle of the platform has little influence on the

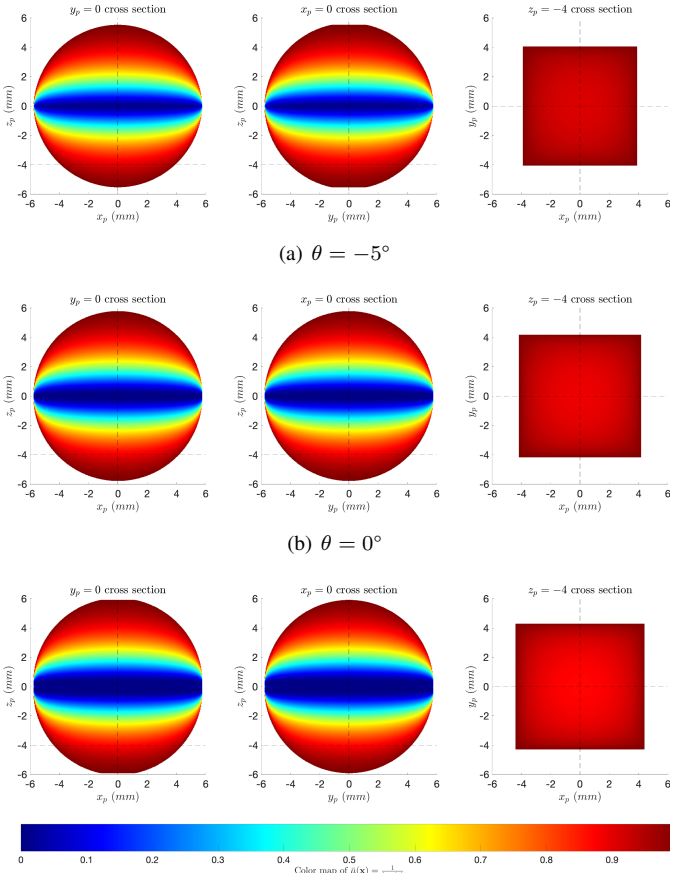

(a) $\theta = -5°$

(b) $\theta = 0°$

(c) $\theta = 5°$

Fig. 9. Cross section of the workspace of the MiGriBot for different values of θ. The color map corresponds to the inverse manipulability index $\bar{\mu}(\mathbf{x})$.

workspace. The global shape of the workspace is a Steinmetz bycylinder (intersection of two cylinders). When $\theta = 0$, its total height and width are exactly two times the length of the legs. Actually, the length of the legs is the unique parameter influencing the size of the workspace when the strokes of the motors are infinite and for a constant θ. In practice, the strokes of the actuator could limit the workspace and they should be carefully chosen to get the largest workspace, as proposed in the workspace optimization section below.

In Figure 9, the color of each point is a function of the manipulability index [28] defined as:

$$\mu(\mathbf{x}) = \sqrt{det(\mathbf{J}\mathbf{J}^{\mathrm{T}})} \tag{30}$$

To homogenize the Jacobian matrix $\mathbf{J}$, the angle of the platform has been expressed as a displacement. To do so, the opening of the gripper η, i.e. the distance between the two fingers has been used in place of the angle θ. η is defined by:

$$\eta = \eta_o + 2n\theta \tag{31}$$

where η_o is the initial gap between the fingers of the gripper and n is the length of each finger. For the MiGriBot, η_o=0.03 mm and n=2.37 mm.

Nevertheless, the manipulability index can take values between 0 (no transmission of joint movements) and $+\infty$

(infinite amplification of joint movement). As both cases are present in the workspace, it is difficult to find a convenient color scale for plotting the index. In consequence, the color of points in Figure 9 has been calculated with the following rule:

$$\bar{\mu}(\mathbf{x}) = \frac{1}{1+\mu} \tag{32}$$

With this rule, an infinite amplification of movements is represented by 0 and no transmission of movements is represented by 1.

In Figure 9 we retrieve the singularities that we found in the analytic analysis. The lowest and highest points of the workspace correspond to the type III singularities (in dark red). The area close to $z_p = 0$ of the workspace contains the type II singularities (in dark blue). Concretely, the workspace is separated into two sub-workspaces (downer part and upper part), considering the horizontal frontier $z_p = 0$. In both parts, the singularities are only close to the frontiers and the whole sub-workspace can be used.

V. Optimal Design

The global workspace previously presented is, most of time, not feasible in practice because of two reasons: the actuators may not have sufficient strokes, and the spherical joints may also have limited ranges of rotation in some directions. Furthermore, the type II and III singularities must be avoided. As the MiGriBot is dedicated to pick-and-place operations, we consider in this section the down part of the workspace only.

The goal of this section is to propose some design rules in order to find the best home position for a given value of motor stroke. In order to provide generic rules whatever the scale considered, we consider adimensional parameters dividing all the dimensions by the limb length l such as $\tilde{q}_i = q_i/l$, $\tilde{u} = u/l$, $\tilde{w} = w/l$, etc.

A. Design Parameters

The actuators will be characterized by two new parameters defining the stroke and the position of the four actuators.

First, we note c (resp. $\tilde{c} = c/l$) the stroke of the four actuators. Then, we define $\mathbf{x_0} = (0; 0; z_0; 0)$ (resp. $\tilde{\mathbf{x}}_\mathbf{0} = (0; 0; \tilde{z}_0; 0)$) as the home position of the manipulator. Using the IKM, we can compute the corresponding joint home adimensional positions:

$$\begin{cases} \tilde{q}_{1_0} &= \tilde{u} + \sqrt{1 - \tilde{z_0}^2} \\ \tilde{q}_{2_0} &= \tilde{w} + \sqrt{1 - \tilde{z_0}^2} \\ \tilde{q}_{3_0} &= -\tilde{u} - \sqrt{1 - \tilde{z_0}^2} \\ \tilde{q}_{4_0} &= -\tilde{w} - \sqrt{1 - \tilde{z_0}^2} \end{cases} \tag{33}$$

We assume that the home joint position corresponds to the neutral positions of the motors, or in other words to the middle of their stroke. It means that $\tilde{q}_{i_0}$ is the offset between the absolute adimensional joint position $\tilde{q}_i$ and the motor relative adimensional position $\tilde{\delta}_i$ following:

$$\tilde{q}_i = \tilde{q}_{i_0} + \tilde{\delta}_i \quad \text{with} \quad \tilde{\delta}_i \in \left[-\frac{\tilde{c}}{2}; \frac{\tilde{c}}{2}\right] \tag{34}$$

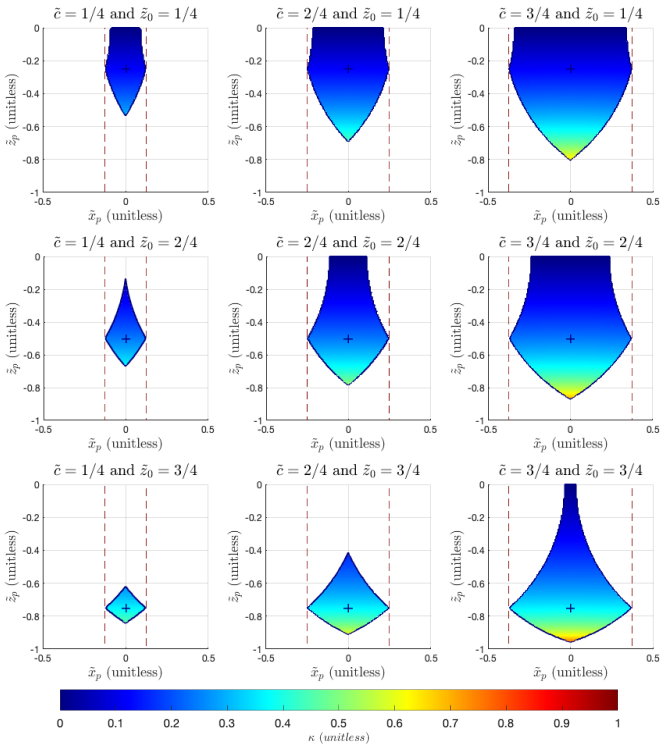

Fig. 10. Adimensional cross sections of the workspace for $y_p = 0$, $\theta = 0$ and for different values of the adimensional stroke $\tilde{c} = c/l$ and adimensional home position $\tilde{z}_0 = z_0/l$. The crosses show the home positions. The vertical red dashed lines are spaced of $\tilde{c}$.

Figure 10 illustrates the influence of the actuator's parameters $\tilde{c} = c/l$ and $\tilde{z_0} = z_0/l$ on the shape of the adimensional workspace (considering $\tilde{x_p}$, $\tilde{y_p}$, $\tilde{z_p}$). It shows that for a given stroke $\tilde{c}$, the home position $\tilde{z_0}$ should be carefully chosen to have a large workspace. Nevertheless, the width of the adimensional workspace along $\tilde{x_p}$ is always equal to $\tilde{c}$ while its height is a function of both parameters of the actuators ($\tilde{c}$, $\tilde{z_0}$).

B. Analysis of the Conditioning Number

In order to select the best workspace for a given stroke, we filled the workspace with a color corresponding to the inverse of the conditioning number [29] defined by:

$$\kappa = \sqrt{\frac{\lambda_{min}(\mathbf{G}\mathbf{G}^\mathrm{T})}{\lambda_{max}(\mathbf{G}\mathbf{G}^\mathrm{T})}} \tag{35}$$

where $\mathbf{G}$ is the submatrix composed of the first three lines of $\mathbf{J}$. λ_{max} and λ_{min} are functions giving the maximum and minimum eigenvalues of a matrix respectively.

The index κ is normalized between 0 and 1. It represents the capacity to homogeneously translate the robotic structure in space. A value close to 1 indicates a homogeneous control of the manipulator along the three directions while a zero indicates a singularity.

In Figure 10, we can see that the lowest the home position $\tilde{z_0}$ is, the highest κ is. As the purpose of MiGriBot is to do fast pick-and-place operations, it is important to have a wide range of motion in $\mathbf{x_w}$ and $\mathbf{y_w}$ directions with homogeneous

transmission ratios. Thus, the bottom-right case is the best choice. This favorable situation happens when the height of the workspace is maximum. In the next section, we will study the impact of the actuator's parameters ($\tilde{c}$, $\tilde{z_0}$) on the height of the workspace.

C. Analysis of the Height of the Workspace

To establish an expression of the height of the workspace, we first use the FKM. Equation (11) shows that $q_1 = -q_3$ and $q_2 = -q_4$ when $x_p = 0$ and $y_p = 0$. Then, by using the FKM and in particular Eq. (21), we obtain after some developments an expression of ${\tilde{z_p}}^2$ as a function of $\tilde{z_0}$, and $\tilde{\delta_2}$:

$${\tilde{z_p}}^2 = {\tilde{z_0}}^2 + 2\tilde{\delta_2}\sqrt{1-{\tilde{z_0}}^2} - {\tilde{\delta_2}}^2 \tag{36}$$

As $\tilde{\delta_2} \in [-\tilde{c}/2; \tilde{c}/2]$, this quadratic equation gives different expressions of the minimum and maximum values of $\tilde{z_p}$ according to the position of its roots and of the vertex of the corresponding parabola. The adimensional height of the workspace $\tilde{h}$ will be defined by doing the difference between the maximal height $\tilde{z}_{max}$ and the minimal one $\tilde{z}_{min}$:

$$\tilde{h} = \tilde{z}_{max} - \tilde{z}_{min} \tag{37}$$

To calculate the minimal position, two different cases have to be considered: if $\sqrt{1-{\tilde{z_0}}^2} < \tilde{c}/2$, the extreme point of the parabola is reach in $[0; \tilde{c}/2]$. It means that the manipulator is able to reach the bottom of the maximal workspace ($\tilde{z_p} = -1$) of Figure 9. Otherwise, the manipulator cannot reach this point and the lowest accessible position is reached when $\tilde{\delta_2} = -\tilde{\delta_4} = \tilde{c}/2$. Thus, we have:

$$\tilde{z}_{min} = \begin{cases} -1 & \text{if } \sqrt{1-{\tilde{z_0}}^2} < \frac{\tilde{c}}{2} \\ -\sqrt{{\tilde{z_0}}^2 + \tilde{c}\sqrt{1-{\tilde{z_0}}^2} - \left(\frac{\tilde{c}}{2}\right)^2} & \text{else} \end{cases} \tag{38}$$

In the same way, to calculate the maximal position, two different cases are considered: if $\sqrt{1-{\tilde{z_0}}^2} > 1 - \tilde{c}/2$, the lowest root of the quadratic equation is in $[-\tilde{c}/2; \tilde{c}/2]$ meaning that the manipulator can reach the plane $O\mathbf{x_w y_w}$ ($\tilde{z_p} = 0$). Otherwise, the manipulator can't reach this point and the highest point is reached when $\tilde{\delta_2} = -\tilde{\delta_4} = -\tilde{c}/2$. So, we get:

$$\tilde{z}_{max} = \begin{cases} 0 & \text{if } \sqrt{1-{\tilde{z_0}}^2} > 1 - \frac{\tilde{c}}{2} \\ -\sqrt{{\tilde{z_0}}^2 - \tilde{c}\sqrt{1-{\tilde{z_0}}^2} - \left(\frac{\tilde{c}}{2}\right)^2)} & \text{else} \end{cases} \tag{39}$$

The three last equations (37), (38), (39) define $\tilde{h} = h/l$ and allow us to study and maximize the height of the accessible workspace whatever the length limb l is.

The values of $\tilde{h}$ as a function of the actuator's parameters $\tilde{c}$ and $\tilde{z_0}$ are presented in Figure 11. It can be divided into three parts corresponding to both previous cases. In part (a), the accessible height increases with the stroke of motors. However, the stroke is not sufficient to go through the whole height of the maximal workspace and the manipulator is not able to reach its lowest point. In area (b), the manipulator is not able to reach the plane $O\mathbf{x_w y_w}$ ($z_p = 0$) which considerably reduces the accessible height. In part (c), the stroke is sufficient to go through the whole height of the maximal workspace ($\tilde{h} = h/l = 1$).

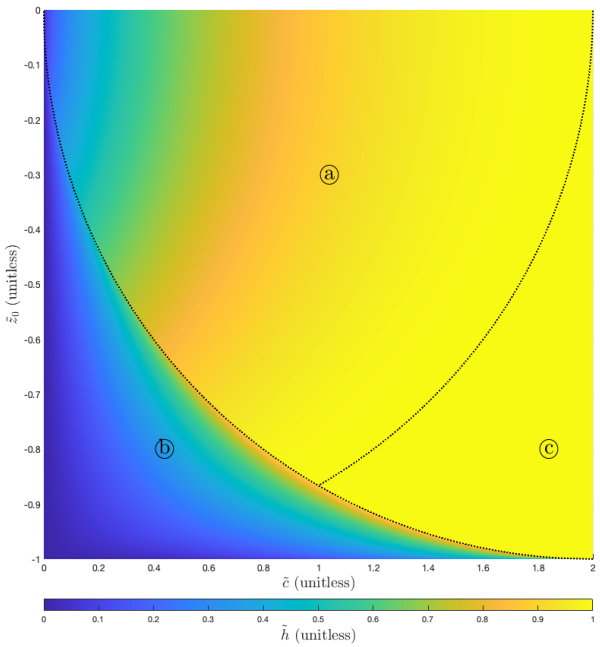

Fig. 11. Adimensional graph representing the height $\tilde{h} = h/l$ of the workspace as a function of $\tilde{c} = c/l$ and $\tilde{z_0} = z_0/l$. The maximal value of $\tilde{h}$ is obtained on the dashed line if $\tilde{c} \leq 1$ and between the dashed lines if $\tilde{c} > 1$.

D. Maximization of the Workspace Height

The non-dimensional analysis enables also to define the home position ${\tilde{z_0}}^*$ that maximizes the workspace height $\tilde{h}$ with regard to $\tilde{c}$. The optimization problem is then:

$$\underset{\tilde{z_0}}{\text{maximize}} \quad h(\tilde{z_0}, \tilde{c}) \tag{40}$$

$$\text{subject to} \quad -1 \leq \tilde{z_0} < 0 \tag{41}$$

When $\tilde{c} \leq 1$, the unique solution of this problem is given by:

$${\tilde{z_0}}^* = -\sqrt{\tilde{c} - \left(\frac{\tilde{c}}{2}\right)^2} \tag{42}$$

This solution corresponds to the dashed curve over part (b) in Figure 11.

When $1 < \tilde{c} \leq 2$ all the points of part (c) maximize the workspace height, and then:

$$-\sqrt{\tilde{c} - \left(\frac{\tilde{c}}{2}\right)^2} \leq {\tilde{z_0}}^* \leq -\sqrt{1 - \left(\frac{\tilde{c}}{2}\right)^2} \tag{43}$$

Finally, if $2 < \tilde{c}$, all values of $\tilde{z_0}$ (in $[-1; 0]$) maximize the workspace height.

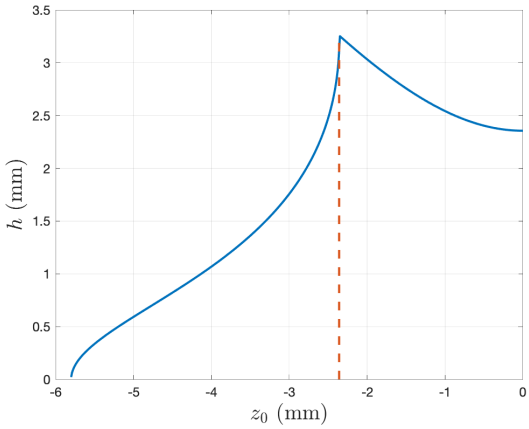

Fig. 12. Workspace height h according to the home position z_0 with the geometric parameters of the MiGriBot ($l = 5.8$ mm and $c = 1$ mm).

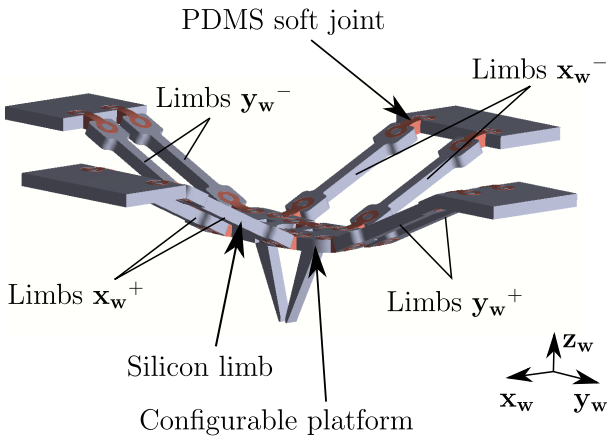

Fig. 13. The MiGriBot parallel mechanism with 18 soft joints [16].

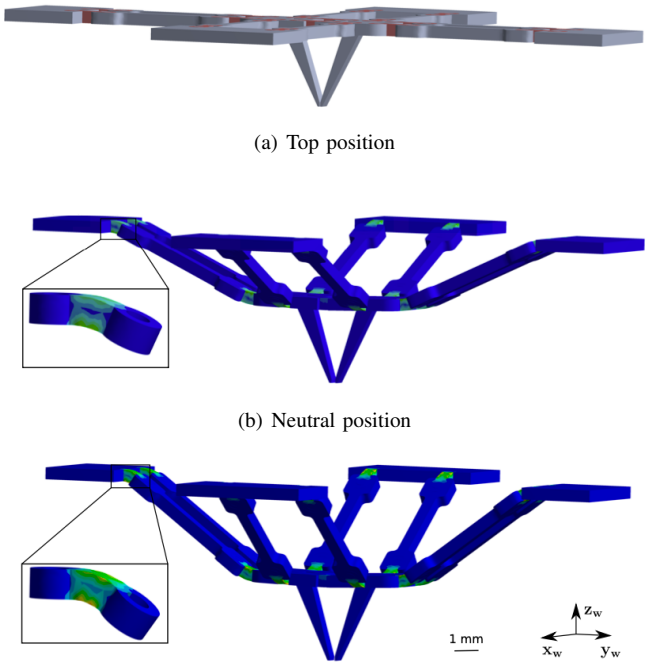

(a) Top position

(b) Neutral position

(c) Down position

Fig. 14. Stress inside the soft joints calculated by the reference A_{fine} model along a pure vertical trajectory (all the actuators receive the same inputs).

E. Numerical Example

To illustrate the workspace height maximisation, we consider the dimension reported in [16], where $l = 5.8$ mm and $c = 1$ mm, meaning $\tilde{c} = 0.17$. Figure 12 shows the workspace height h as a function of the home position z_0. The maximum height is indeed reached for $z_0 = -2.36$ mm meaning $\tilde{z_0} = -0.41$ as predicted by Eq. (42). This home position corresponds to a workspace that touches the plane $O\mathbf{x_w}\mathbf{y_w}$ in only one point at its top. Thus, taking a home position a few lower than this one prevents the manipulator from reaching type II singularity that could lead to a change of its orientation or a breakage.

VI. Simulations and Experiments

To assess the accuracy of the proposed model ($C_{spherical}$), we compared it with two different models and with experimental results. The first model was obtained by considering the soft joints as 1D beam elements using the BeamAdapter plugin of SOFA (S_{1D}). The second model is obtained by FEM where the PDMS joints are discretized as 3D elements using ANSYS© (A_{fine}). Since the soft joints might be subject to large deformations, a nonlinear model with quadratic interpolations and regular 3D 40 µm tetrahedrons meshing were implemented. The silicon parts, considered as significantly more rigid than the soft joints, were modeled using 200 µm hexahedral meshing.

A. Simulation of a vertical trajectory

The considered robotic architecture illustrated in Fig. 13, is a parallel mechanism composed of 18 soft cubic joints (size ratio of 1) made of PDMS (polydimethylsiloxane) and 14 rigid links made of silicon [16]. Each part has a constant thickness of 0.4 mm and each silicon link has a length of 5 mm.

The four legs of the robot are moved toward the center position making the platform go down. Looking at the vertical motion of the platform according to the actuator positions presented in Fig. 15, we can see that the positions predicted by the three tested models ($C_{spherical}$, S_{1D} and A_{fine}) are close to each other. The computational time goes from 0.9 ms for the rigid-body model $C_{spherical}$ to 6300 s for the 3D FEM model A_{fine}. The maximal position error between them is 7.6% for a travel range of 2.1 mm. The deviation can be explained by the fact that the A_{fine} model is more accurate when compared to the two others (see Fig. 14).

Compared to the real experiments, the three models give an overestimation of z_w on the highest positions and an underestimation on the lowest positions. In other words, the movement of the real robot has a smaller amplitude than expected. The maximal position error is 16.0% at the highest position. This is most likely due to the assembly errors. However, in the central part of the workspace, where the robot is most used for pick-and-place operations, the different models are closer to the experimental measurements. Finally, one can notice that

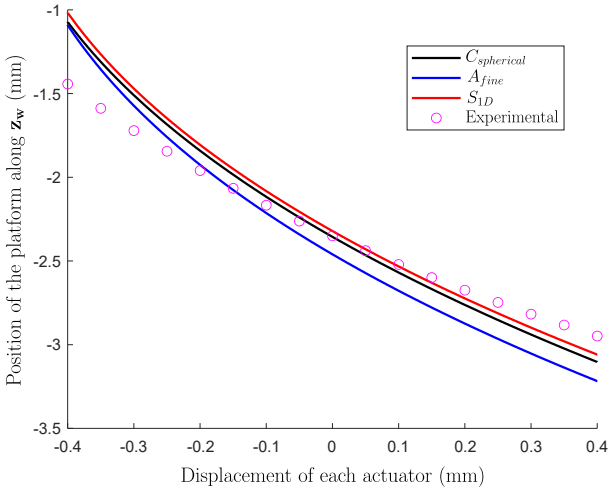

Fig. 15. Comparison between the experimental and the predicted positions by the $C_{spherical}$, S_{1D}, and A_{fine} models along a pure vertical trajectory (all the actuators receive the same inputs).

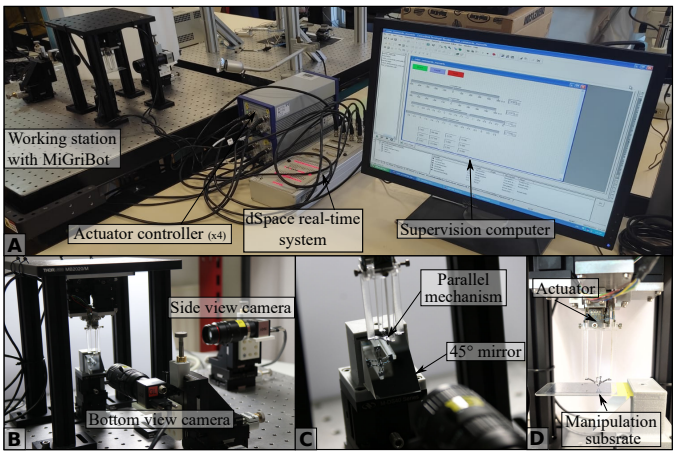

Fig. 16. Experimental setup. A- Complete experimental setup, including the supervision computer, the dSpace real-time system, the four actuator controllers, and the working station integrating MiGriBot. B- Camera positioning for capturing side and bottom views; the side-view camera was replaced with a high-speed camera when required. C- Configuration of the bottom-view generation using a 45° mirror. D- MiGriBot and the manipulation substrate used in experiments.

the beam and the FEM models do not perform really better than the proposed model while being significantly slower. Using these more complex models while expecting better performances is thus not necessarily empirically justified.

B. Experimental validation of a pick-and-place trajectory

An overview of the experimental setup and MiGriBot's working environment is illustrated in Fig. 16 including the supervision computer, the dSpace real-time system, the four actuator controllers, and the working station integrating MiGriBot. Fig. 16.B details the positioning of cameras used for capturing side and bottom views of the manipulator.

For bottom-view imaging, a 45° mirror was placed beneath the parallel mechanism, as illustrated in Fig. 16.C. The final part of the experimental setup is the manipulation substrate, located between the parallel mechanism and the mirror (see Fig. 16.D).

The control architecture of MiGriBot consists of three main components: the dSpace real-time system, the four actuator controllers, and MiGriBot itself. The first component (highlighted in red in Fig. 17) includes a dSpace real-time controller, programmed using Matlab/Simulink, which handles the real-time trajectory generation. The second component (shown in blue in Fig. 17) comprises the actuator controllers from Physik Instrumente GmbH, which operate in closed-loop mode with position sensors for each actuator. The third component (indicated in green in Fig. 17) is MiGriBot, which includes the parallel mechanism and the actuation system.

The control system takes as input the target position of MiGriBot. The dSpace real-time system then generates a trajectory between the target and the current position, following a trapezoidal velocity profile. The Cartesian coordinates are subsequently converted into joint-space coordinates using the inverse kinematics model presented in this paper, which is implemented in the dSpace real-time system.

The computed joint position vector is transmitted to the actuator controllers, which drive each piezoelectric actuator to achieve the desired displacement. Position sensors provide feedback on the actuator positions, enabling precise position control through a closed-loop system.

Finger position measurements for trajectory analysis and positioning repeatability evaluation were obtained using image correlation during post-processing. Due to the long focal lengths of the macro lenses, an orthographic projection model was applied. The scale was determined using visible dot grids on the fingers and the known link lengths of the robot for bottom-view measurements. All displacements were tracked using template matching.

To analyze the accuracy of the proposed model during realistic tasks, we define a reference trajectory, shown in black in Fig. 18, consisting of a U-cycle with a constant gripper opening. The inverse kinematics of the rigid-body model, $C_{spherical}$, was used to compute the four actuator inputs. These inputs were used in the experiments (where circles represent the measured positions of the end-effector) and for all models (where lines indicate the predicted trajectory of the end-effector).

Regarding the trajectory in the x_w, y_w plane (see Fig. 18), the three models ($C_{spherical}$, S_{1D}, and A_{fine}) predict very similar behavior. The maximum position error among the three models is 4.5

As for the vertical motion, all the models overestimate the z_w elevation. The maximal position error is 10.8% between the A_{fine} model and the experiments. These results confirm that the proposed spherical joint model represents a relevant compromise between the model accuracy and speed.

VII. Conclusion

In this paper, we demonstrate that cubic miniaturized soft joints can effectively function as spherical joints for the design and modeling of miniaturized parallel robots. We show that

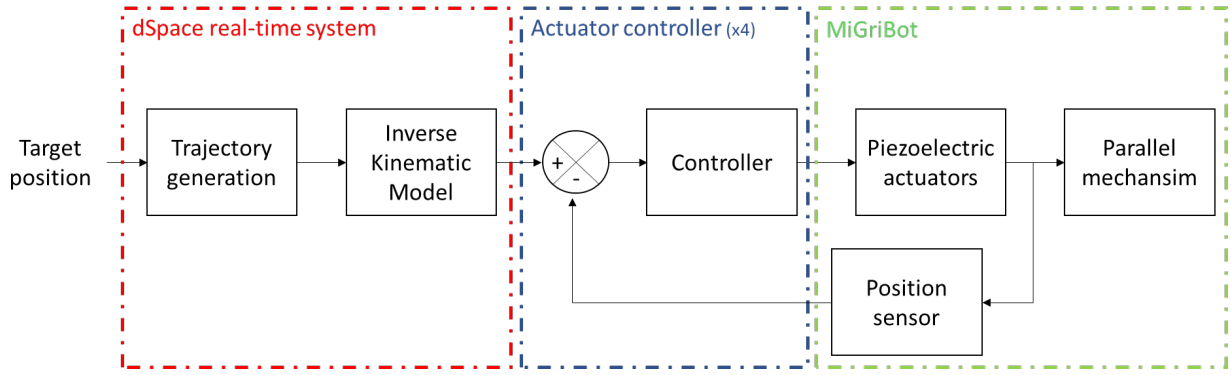

Fig. 17. Block diagram of the control architecture of MiGriBot. The control system transforms the target position into actuator displacements and deformations of the parallel mechanism. It consists of three main components: the dSpace real-time system, the actuator controller, and MiGriBot.

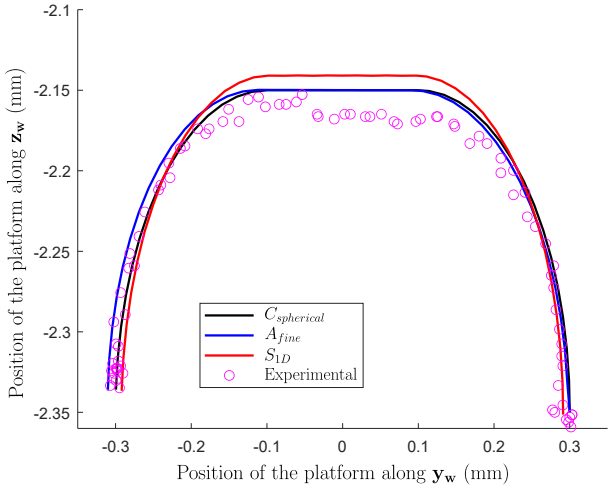

Fig. 18. Comparison between the experimental and the predicted positions by the $C_{spherical}$, S_{1D}, and A_{fine} models along a U-Shape trajectory in the $y_w; z_w$ plane.

models derived from this approximation are comparable in accuracy to FEM while enabling high-speed computation (over 1 kHz on a standard PC) and real-time control. This approach also simplifies the analysis and optimization of the mechanism, paving the way for designing complex, miniaturized robotic architectures with unprecedented precision and speed. The soft joint approach not only allows miniaturized robots to achieve high speeds, as demonstrated by MiGiBot (12 pick-and-place operations per second), but also enables real-time adaptation to manipulation tasks. In addition to the implementation of high-speed feedback control of the robot, allowing it to adapt to its environment, future work will focus on optimizing the soft joint beyond cuboid shapes using topology optimization to further enhance its behaviour and the accuracy of its model both at the micro and the macro scales.

APPENDICES

A. Appendix A

The stiffness matrix K of a beam element is given by:

$$\begin{pmatrix} \frac{AE}{L} & 0 & 0 & 0 & 0 & 0 \\ 0 & \frac{12EI_z}{L^3(1+\alpha_y)} & 0 & 0 & 0 & \frac{6EI_z}{L^2(1+\alpha_y)} \\ 0 & 0 & \frac{12EI_y}{L^3(1+\alpha_z)} & 0 & -\frac{6EI_y}{L^2(1+\alpha_z)} & 0 \\ 0 & 0 & 0 & \frac{GJ}{L} & 0 & 0 \\ 0 & 0 & -\frac{6EI_y}{L^2(1+\alpha_z)} & 0 & \frac{EI_y(4+\alpha_z)}{L(1+\alpha_z)} & 0 \\ 0 & \frac{6EI_z}{L^2(1+\alpha_y)} & 0 & 0 & 0 & \frac{EI_z(4+\alpha_y)}{L(1+\alpha_y)} \end{pmatrix} \tag{44}$$

with E the Young's modulus, G the shear modulus, $A = L^2$ the cross-sectional area, L the joint length, I_y and I_z the second moments of area, α_y and α_z the shear-deformation parameters.

B. Appendix B

The coordinates of the points A_1, P_1, P_2 and B_1 verify:

$$A_1 = \begin{pmatrix} \frac{AB}{2} + 2.5 \\ 0 \\ 0 \end{pmatrix}, \quad P_1 = \begin{pmatrix} -1.25 \\ 0 \\ z_p \end{pmatrix},$$
$$B_1 = \begin{pmatrix} -\frac{AB}{2} - 2.5 \\ 0 \\ 0 \end{pmatrix}, \quad P_2 = \begin{pmatrix} 1.25 \\ 0 \\ z_p \end{pmatrix}. \tag{45}$$

Two geometric closure equations related to the two legs, of length l, can be written:

$$l^2 = \left(\frac{AB}{2} + 3,75\right)^2 + {z_p}^2 \tag{46}$$

This equation enables us to derive the forward and inverse kinematics that link the controlled length AB and the elevation z_p of the points P_1 and P_2.

REFERENCES

[1] M. Sitti, "Microscale and nanoscale robotics systems [grand challenges of robotics]," *IEEE Robotics & Automation Magazine*, vol. 14, no. 1, pp. 53–60, 2007.

[2] G.-Z. Yang, J. Bellingham, P. E. Dupont, P. Fischer, L. Floridi, R. Full, N. Jacobstein, V. Kumar, M. McNutt, R. Merrifield, *et al.*, "The grand challenges of science robotics," *Science robotics*, vol. 3, no. 14, p. eaar7650, 2018.

[3] M. Gauthier, P. Lambert, and S. Régnier, "Microhandling and micromanipulation strategies," *Microrobotics for micromanipulation*, pp. 179–242, 2013.

[4] D. Hériban and M. Gauthier, "Robotic micro-assembly of microparts using a piezogripper," in *2008 IEEE/RSJ international conference on intelligent robots and systems*, pp. 4042–4047, IEEE, 2008.

[5] Z. Lyu and Q. Xu, "Recent design and development of piezoelectric-actuated compliant microgrippers: A review," *Sensors and Actuators A: Physical*, vol. 331, p. 113002, 2021.

[6] R. Li and H. Qiao, "A survey of methods and strategies for high-precision robotic grasping and assembly tasks—some new trends," *IEEE/ASME Transactions on Mechatronics*, vol. 24, no. 6, pp. 2718–2732, 2019.

[7] D. Farhadi Machekposhti, N. Tolou, and J. Herder, "A review on compliant joints and rigid-body constant velocity universal joints toward the design of compliant homokinetic couplings," *Journal of Mechanical Design*, vol. 137, no. 3, p. 032301, 2015.

[8] S. Linß, S. Henning, and L. Zentner, "Modeling and design of flexure hinge-based compliant mechanisms," in *Kinematics-Analysis and Applications*, IntechOpen, 2019.

[9] L. L. Howell, "Compliant mechanisms," in *21st century kinematics*, pp. 189–216, Springer, 2013.

[10] J. E. Correa, J. Toombs, N. Toombs, and P. M. Ferreira, "Laminated micro-machine: Design and fabrication of a flexure-based delta robot," *Journal of Manufacturing Processes*, vol. 24, pp. 370–375, 2016.

[11] D. E. Vogtmann, S. K. Gupta, and S. Bergbreiter, "Characterization and Modeling of Elastomeric Joints in Miniature Compliant Mechanisms," *Journal of Mechanisms and Robotics*, vol. 5, Oct. 2013.

[12] A. DeMario and J. Zhao, "Development and analysis of a three-dimensional printed miniature walking robot with soft joints and links," *Journal of Mechanisms and Robotics*, vol. 10, no. 4, 2018.

[13] A. Bruyas, F. Geiskopf, L. Meylheuc, and P. Renaud, "Combining multi-material rapid prototyping and pseudo-rigid body modeling for a new compliant mechanism," in *2014 IEEE International Conference on Robotics and Automation (ICRA)*, pp. 3390–3396, IEEE, 2014.

[14] R. S. Pierre, N. Paul, and S. Bergbreiter, "3dflex: A rapid prototyping approach for multi-material compliant mechanisms in millirobots," in *2017 IEEE International Conference on Robotics and Automation (ICRA)*, pp. 3068–3073, IEEE, 2017.

[15] C. Aygül, J. Kwiczak-Yiğitbaşi, B. Baytekin, and O. Özcan, "Joint design and fabrication for multi-material soft/hybrid robots," in *2019 2nd IEEE International Conference on Soft Robotics (RoboSoft)*, pp. 477–482, IEEE, 2019.

[16] M. Leveziel, W. Haouas, G. J. Laurent, M. Gauthier, and R. Dahmouche, "Migribot: A miniature parallel robot with integrated gripping for high-throughput micromanipulation," *Science Robotics*, vol. 7, no. 69, p. eabn4292, 2022.

[17] Z. Yang, B. Jeong, A. Vakakis, and S. Kim, "A tip-tilt-piston micromirror with an elastomeric universal joint fabricated via micromasonry," *Journal of Microelectromechanical Systems*, vol. 24, no. 2, pp. 262–264, 2015.

[18] W. Haouas, R. Dahmouche, J. Agnus, N. Le Fort-Piat, and G. J. Laurent, "New integrated silicon-pdms process for compliant micromechanisms," *Journal of Micromechanics and Microengineering*, vol. 27, no. 12, p. 127001, 2017.

[19] H. McClintock, F. Z. Temel, N. Doshi, J.-s. Koh, and R. J. Wood, "The millidelta: A high-bandwidth, high-precision, millimeter-scale delta robot," *Science Robotics*, vol. 3, no. 14, 2018.

[20] E. Coevoet, T. Morales Bieze, F. Largilliere, Z. Zhang, M. Thieffry, M. Sanz Lopez, B. Carrez, D. Marchal, O. Goury, J. Dequidt, and C. Duriez, "Software toolkit for modeling, simulation and control of soft robots," *Advanced Robotics*, vol. 31, pp. 1208–1224, Nov. 2017.

[21] V. K. Venkiteswaran and H.-J. Su, "A Three-Spring Pseudorigid-Body Model for Soft Joints With Significant Elongation Effects," *Journal of Mechanisms and Robotics*, vol. 8, 06 2016. 061001.

[22] H. Suzuki and R. J. Wood, "Origami-inspired miniature manipulator for teleoperated microsurgery," *Nature Machine Intelligence*, vol. 2, no. 8, pp. 437–446, 2020.

[23] S. Mintchev, M. Salerno, A. Cherpillod, S. Scaduto, and J. Paik, "A portable three-degrees-of-freedom force feedback origami robot for human–robot interactions," *Nature Machine Intelligence*, vol. 1, no. 12, pp. 584–593, 2019.

[24] I. Miranda, A. Souza, P. Sousa, J. Ribeiro, E. M. Castanheira, R. Lima, and G. Minas, "Properties and applications of pdms for biomedical engineering: A review," *Journal of functional biomaterials*, vol. 13, no. 1, p. 2, 2021.

[25] A. Müller, M. C. Wapler, and U. Wallrabe, "A quick and accurate method to determine the poisson's ratio and the coefficient of thermal expansion of pdms," *Soft Matter*, vol. 15, no. 4, pp. 779–784, 2019.

[26] E. Berthier, E. W. Young, and D. Beebe, "Engineers are from pdms-land, biologists are from polystyrenia," *Lab on a Chip*, vol. 12, no. 7, pp. 1224–1237, 2012.

[27] C. Gosselin and J. Angeles, "Singularity analysis of closed-loop kinematic chains," *IEEE Transactions on Robotics and Automation*, vol. 6, no. 3, pp. 281–290, 1990.

[28] T. Yoshikawa, "Manipulability of robotic mechanisms," *The international journal of Robotics Research*, vol. 4, no. 2, pp. 3–9, 1985.

[29] J.-P. Merlet, "Jacobian, manipulability, condition number, and accuracy of parallel robots," *ASME Journal of Mechanical Design*, vol. 128, pp. 199–206, 01 2006.